Appendix A

Effect of porous texture on hydrogen adsorption in activated carbons

A.1 Introduction

Physisorption-based hydrogen (H_2) storage in microporous carbons has a trade-off between adsorption capacity and adsorption enthalpy [5]. Conceptually, this problem is best illustrated in terms of the ideal slit pore formed from two parallel, semi-infinite graphite slabs. Packing density is maximized when the pore width is several times larger than the diameter of the H_2 molecule, since it permits the formation of several hydrogen monolayers within the pore [16]. At supercritical temperatures, however, condensation within pores does not occur. Characteristic H_2 adsorption enthalpies associated with large slit pores therefore approach the enthalpy of H_2 adsorption on carbon, typically measured between $4\,\mathrm{kJ\,mol^{-1}}$ to $6\,\mathrm{kJ\,mol^{-1}}$ [15, 121]. With smaller pores, the adsorption enthalpy increases due to the overlap of potentials fields from each face of the pore. The packing density begins to decrease, though, when the pore is no longer wide enough to accommodate two H_2 monolayers. *Ab initio* calculations of hydrogen adsorption in ideal slit pore carbons

Portions of this chapter were published in the article: J. J. Purewal, H. Kabbour, J. J. Vajo, C. C. Ahn and B. Fultz, *Nanotechnology* **2009**, *20*, 204012.

are largely consistent with this picture [16, 122]. The fundamental limitations of hydrogen storage in activated carbons are difficult to study experimentally because uniform slit pore structures do not occur in nature. To extend the slit pore concept to realistic carbon adsorbents, the distribution of pore sizes must be understood.

Due to their microporosity, activated carbon fibers (ACF) are an excellent material for a fundamental study of H_2 adsorption capacity and enthalpy. ACFs are synthesized from polymeric carbon precursors and contain narrow pore size distributions [6, 123]. Images of ACFs from scanning tunneling microscopy have revealed networks of elongated slit-shaped and ellipsoid-shaped pores [124, 125]. Edge terminations in graphitic layers are thought to be the most reactive sites during the physical activation process, resulting in a gradual lengthening of slit shaped pores as a function of burn-off [126]. ACFs subjected to less burn-off will have smaller pore volumes and a greater abundance of narrow pores widths. With longer activation times, the pores grow larger resulting in a larger amount of mesopores. This offers a convenient control for an experimental study of pore structure and hydrogen adsorption.

In the current study, the pore size distributions (PSD) of ACFs are compared to the hydrogen adsorption enthalpy and adsorption capacity. Two ACF samples subjected to different degrees of activation are characterized. The microstructure of the activated carbon samples is investigated first with high resolution transmission electron microscopy (HRTEM). Then the PSD is obtained from argon adsorption measurements using the density functional theory method. Supercritical hydrogen adsorption isotherms are measured, and the enthalpies and capacities are determined. Measurements are also performed on a microporous, coconut-derived activated carbon as a control sample.

A.2 Experimental Methods

Kynol™ activated carbon fiber samples ACF-1603-10 (ACF-10) and ACF-1603-20 (ACF-20) were obtained from Kynol Inc. These ACFs are produced by carbonization and gasification of a phenolic resin precursor. The last two digits in the labels are an approximate indication of surface area in hundreds of $m^2\,g^{-1}$. The commercial, coconut-shell-derived activated carbon CNS-201 (CNS-201) was purchased from A.C. Carbon Canada Inc. Since CNS-201 is known to be highly microporous (90 % of pores are smaller than 1.3 nm), it is a useful reference material for the microporous ACFs. Textural parameters were obtained from Ar isotherms (87 K) for ACF-10 (0.2811 g) and ACF-20 (0.3222 g), and from a N_2 isotherm (77 K) for CNS-201 (0.1019 g). For illustration, the Ar isotherm for ACF-10 is displayed in Fig. A.1a. Surface areas and saturation pore volumes are calculated from the BET equation, given by

$$\frac{p/p^\circ}{n\,(1-p/p^\circ)} = \frac{1}{n_\mathrm{m}C} + \frac{C-1}{n_\mathrm{m}C}\,(p/p^\circ)\,. \tag{A.1}$$

The monolayer capacity, n_m, is determined from the slope and y-intercept of the fitted line in Fig. A.1c. We can then calculate the BET surface area, a(BET), from the molecular cross-sectional area (σ) using the formula,

$$a(\mathrm{BET}) = n_\mathrm{m} N_\mathrm{a} \sigma, \tag{A.2}$$

where N_a is the Avogadro constant.

Total pore volumes are calculated from the Dubinin-Astakhov equation, given by

$$\log(n) = \log(n_\mathrm{p}) - D\,[\log(p^\circ/p)]^x\,, \tag{A.3}$$

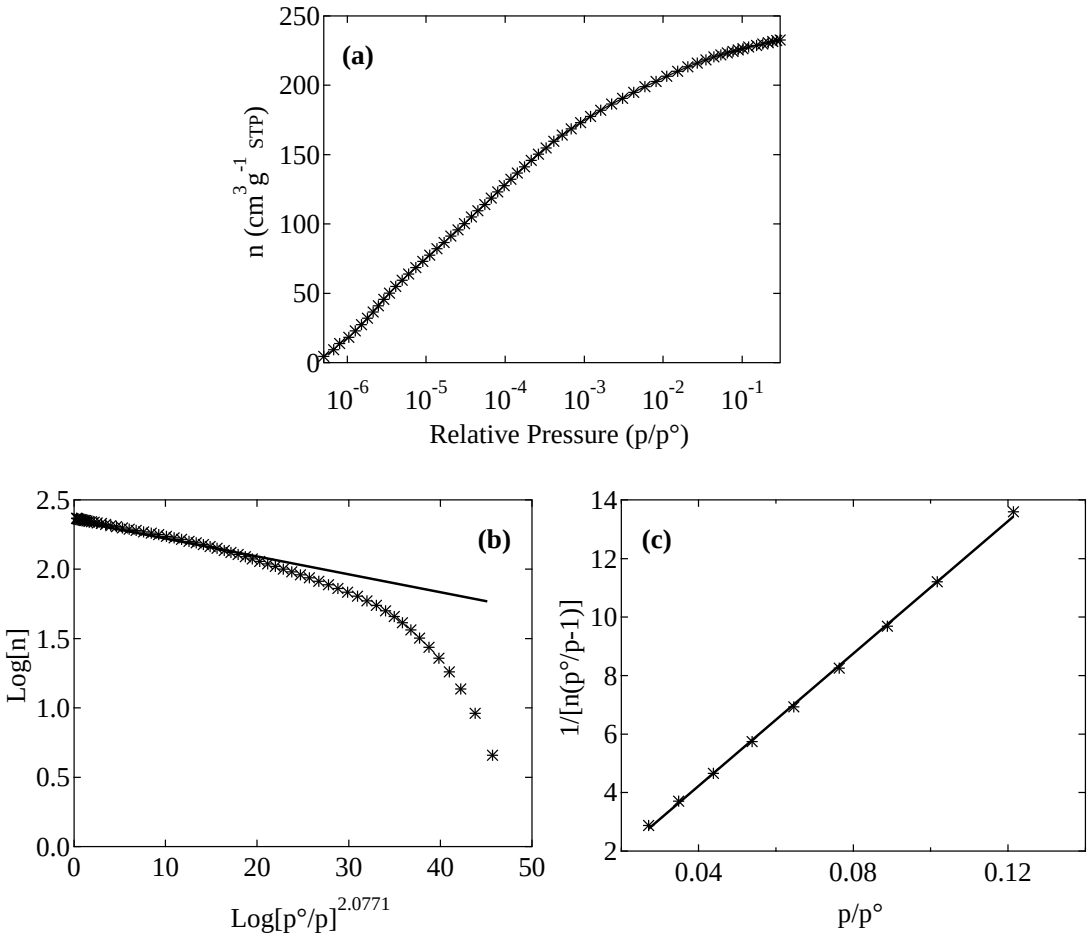

Figure A.1: Surface texture analysis for sample ACF-10. (a) Ar isotherm measured at 87 K. (b) Dubinin-Astakhov transformed isotherm plot. (c) BET surface area plot.

where D are x are empirical constants.[1] The pore capacity, n_{p}, is determined from the y-intercept of the fitted line in Fig. A.1b. It is then used to calculate the pore volume

$$V_{\mathrm{p}} = n_{\mathrm{p}} \times M/\rho, \tag{A.4}$$

where M and ρ are the molar mass and liquid density (at 87 K) of Ar. Pore size distributions were calculated using the original DFT method as implemented in Micromeritics ASAP 2020 Version 3.01 software.[2]

[1] Note that x was optimized as 2.0771 for ACF-10, as indicated on the x-axis of Fig. A.1b.

[2] Ar and N_2 isotherms, and DFT modeling performed by Micromeritics Analytical Services.

High resolution TEM micrographs were acquired on a Tecnai F30-UT operated at 300 keV. Sample preparation consisted of grinding about 10 mg of the sample in isopropanol and dispersing it on a carbon grid. High-pressure H_2 isotherms were measured with the custom-built Sieverts apparatus at temperatures of 77 K, 87 K, and 195 K. This instrument was described in detail in Sec. 3.1.3. The sample weights used for the hydrogen adsorption measurements were 0.1782 g (ACF-10), 0.2114 g (ACF-20) and 0.903 g (CNS-201). Prior to adsorption measurements, samples were degassed by heating at 200 ℃ under vacuum for 12 h. Sample masses were measured again after the adsorption experiment to check for changes in mass due to removal of residual water. The void volume of the sample was estimated by assuming a skeletal density of 2.1 g ml^{-1}, which is typically sufficient for most carbon samples.

A.3 Results

An HRTEM micrograph of ACF-10 is presented in A.2. ACFs are known to be more graphitic than typical activated carbons [126], but this is not obvious from the image. The microstructure appears similar to the highly disordered microstructures typically observed for activated carbons. Micropore structures were not visible in the HRTEM analysis. However, the combination of finite sample thickness and non-periodicity tends to conceal micropore structures.

The BET surface areas and total pore volumes for ACF-10, ACF-20, and CNS-201 are listed in A.1. As expected, ACF-10 (subject to less burn-off than ACF-20) has a smaller pore volume and smaller BET surface area than ACF-20. The activated coconut carbon CNS-201 appears to have a BET surface area and pore volume which is intermediate between the two

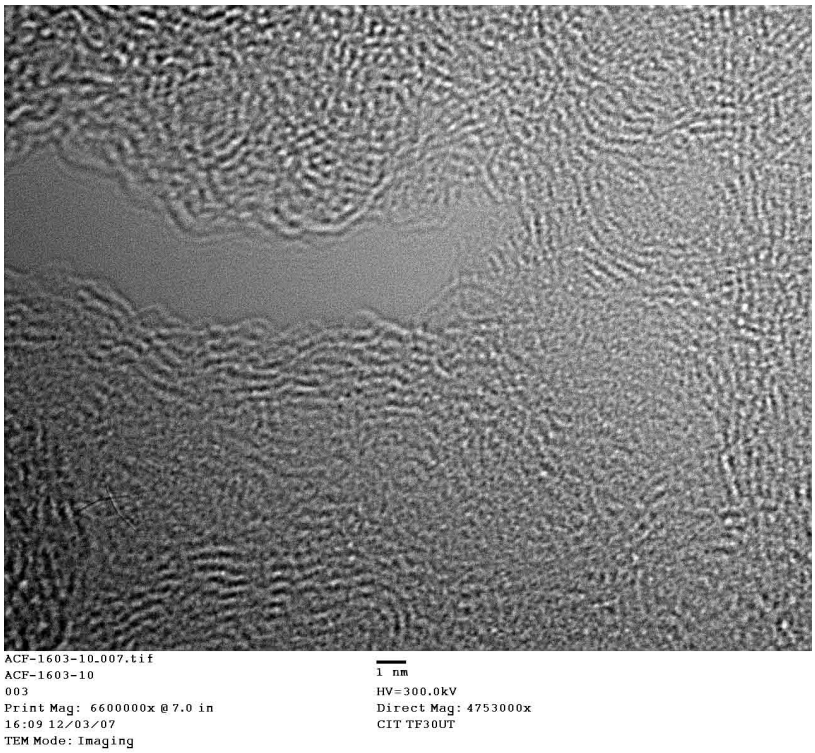

Figure A.2: High-resolution TEM image of ACF-10. Length scale in indicated in the figure.

ACFs.[3] Calculated surface areas of activated carbons are often unrealistically high, since the micropore adsorption mechanism is not equivalent to the multilayer process assumed in the BET model. Nevertheless, the BET method is useful for comparisons between different materials.

Pore size distributions obtained from the DFT method are displayed in Fig. A.3. The pore width is defined as $L - d$, where L is the internuclear spacing between the walls of the slit pore and d is the van der Waals diameter of carbon (3.4 Å). Since graphite has an interlayer spacing of $L = 3.35$ Å, a slit pore formed from a single missing graphene plane has a width of 3.3 Å. A slit pore formed from two missing graphite planes has a width of 6.7 Å, and a pore formed from three missing graphite planes has a width of 10 Å. Taking into account the finite diameter of Ar (2.8 Å) and N_2 (3.0 Å), the cutoff in the pore spectrum

[3]Note that textural parameters were obtained from Ar isotherms for the ACFs and from N_2 isotherms for CNS-201. For direct comparison between samples it would have been better to have used the same adsorptive. Textural parameters obtained by Ar and N_2 data are still sufficient for the qualitative comparison done here.

Table A.1: Surface texture parameters

Sample	SSA $(m^2\,g^{-1})^a$	V_{pore} $(cm^3\,g^{-1})^b$
ACF-10	801	0.296
ACF-20	1817	0.706
CNS-201	1158	0.452

[a] Specific surface areas obtained by the BET method.
[b] Total specific pore volumes obtained from the Dubinin-Astakhov equation.
[c] The textural parameters of ACF-10 and ACF-20 were obtained from Argon measurements at 87 K while those of CNS-201 were obtained from N_2 measurements at 77 K.

must be above 3 Å.[4]

The pore size distributions displayed in Fig. A.3 all show a sharp increase in intensity just below 5.0 Å, which corresponds to a width that is between the predicted pore widths for one or two removed graphite planes. This may simply reflect the smallest pore width which is measurable by the specific probe molecule. Another possibility is that after the removal of two layer planes, the slit pore structure relaxes to the observed 5 Å spacing. The pore distribution of ACF-10 is narrow, consisting of the single large peak at 5 Å. Since burn-off in ACF-10 was minimized, larger pore structures did not develop fully, and are present only as a small tail in the PSD. For ACF-20 there is a broad distribution of pore widths from 5 Å to 20 Å with a small positive skew. Since ACF-20 was subject to a greater degree of burn-off, larger pores were formed during the activation process.[5] The activated carbon CNS-201 also appears to have a distribution of pore widths between 5 Å and 20 Å with a positive skew. This broad distribution of pore widths in ACF-20 and CNS-201 may reflect the presence of slit pores formed from the removal of up to six graphite planes.

[4]Smaller probe molecules, such as helium, could measure pore widths below this cutoff.

[5]The minima near 6 Å and 10 Å are likely to be model-induced artifacts which are independent of the actual sorbent material [127]. The minima in the distributions have been proposed to originate from packing effects where the pore width transitions from being able to support one adsorbed layer to two, and from two layers to three. This width is governed by the functional form used for the adsorbing molecule, for example, a Lennard-Jones potential. However, the fact that the maxima in the distributions are separated by integrals of the graphite layer spacing distance suggests that the maxima may be real and correspond to pores formed from removal of one, two, three, etc, graphitic planes.

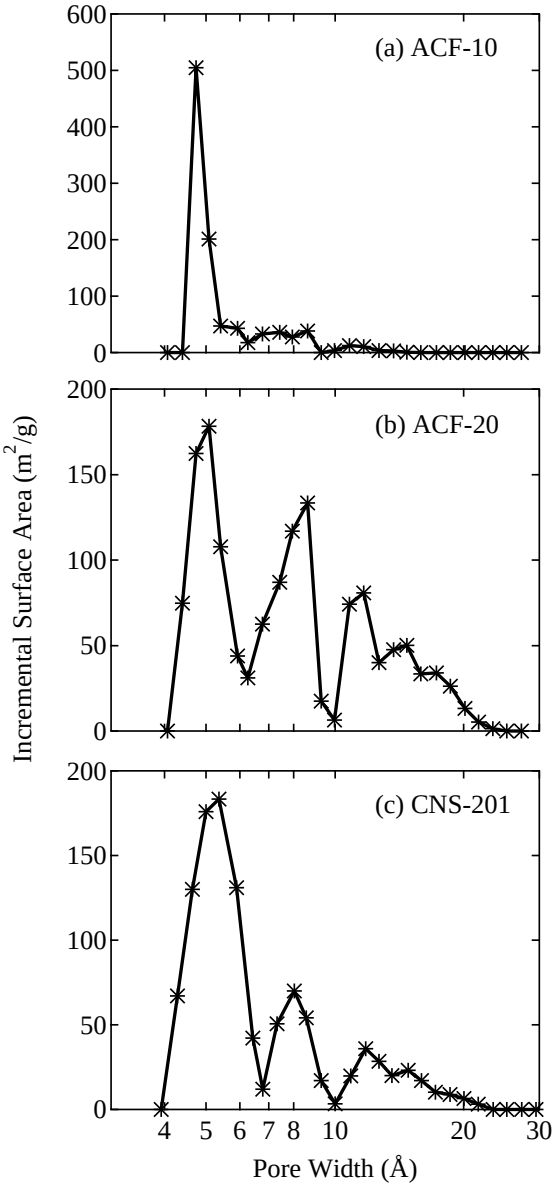

Figure A.3: Pore size distributions determined by the DFT method for (a) ACF-10, (b) ACF-20, and (c) CNS-201. The bottom axis is shown in logarithmic scale.

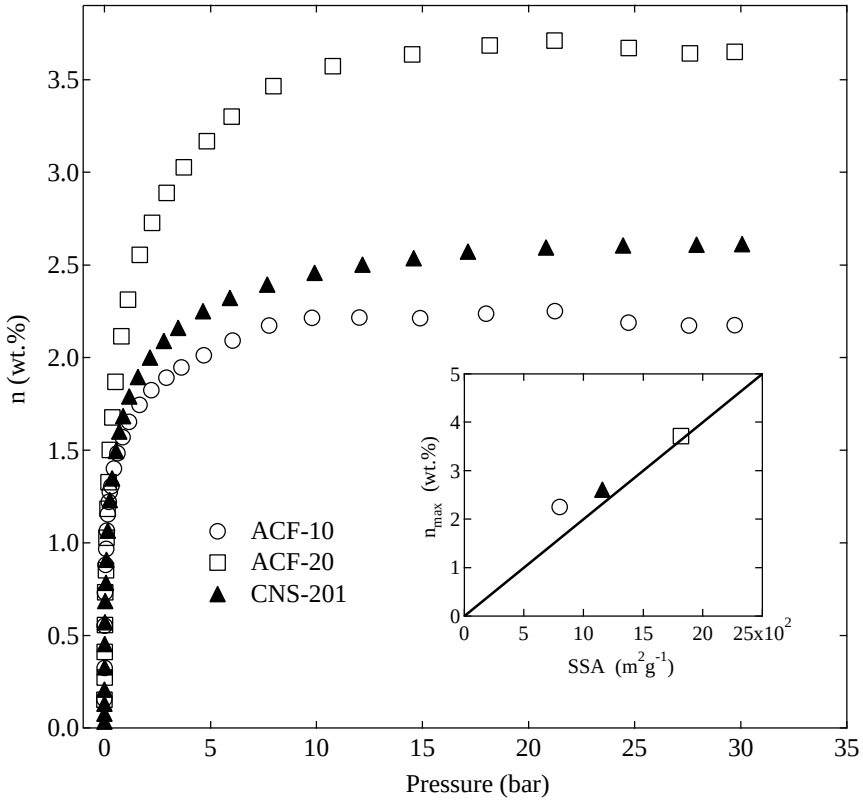

Figure A.4: Hydrogen adsorption isotherms at 77 K for ACF-10, ACF-20, and CNS-201. Inset: Maximum H_2 adsorption capacity (wt%) at 77 K versus BET specific surface area ($m^2\,g^{-1}$), with the solid line signifying a 1 wt% per $500\,m^2\,g^{-1}$ linear relationship.

Supercritical H_2 isotherms are displayed in Fig. A.4. As discussed in Sec. 1.6.7, comprehensive studies of H_2 adsorption in activated carbons typically report a linear dependence of n_{max} at 77 K with specific surface area [19, 20, 128]. An increase of approximately 1 wt% hydrogen for every $500\,m^2\,g^{-1}$ of surface area is the rule-of-thumb. As shown in the inset of Fig. A.4, the hydrogen adsorption capacities of ACF-10, ACF-20, and CNS-201 at 77 K roughly follow the rule-of-thumb, although ACF-10 does show a substantial positive deviation. Since ACF-10 is almost exclusively microporous, with little contribution from mesopores,[6] this may explain why it shows a large positive deviation from the $500\,m^2\,g^{-1}$ per 1 wt% rule. On the other hand, ACF-20 has a wider distribution of both micropores

[6]Small mesopores can produce large BET surface areas, but contribute little to hydrogen adsorption capacity.

Table A.2: Hydrogen adsorption parameters

Sample	$\Delta\dot{h}_0$ (kJ mol^{-1})[a]	ΔH_{avg} (kJ mol^{-1})[b]	n_{max} (wt%)[c]
ACF-10	8.92	6.64	2.1
ACF-20	7.63	5.85	3.5
CNS-201	8.59	6.07	2.5

[a] Enthalpy of hydrogen adsorption in the zero-coverage limit.
[b] Average isosteric heats between 0 wt% and 1.8 wt%.
[c] Maximum hydrogen adsorption capacity at 77 K.

and mesopores, which may explain why it does not show the same positive deviation from the rule-of-thumb.

Accurate adsorption amounts were measured in the low-pressure region using a high-resolution pressure gauge. Henry's law constants were then calculated at 77 K, 87 K, and 195 K from the zero-order virial coefficient $C_0 = \ln(k_H)$ in Eq. 3.11. The differential enthalpy of adsorption was calculated from the temperature variation of k_H using the van't Hoff expression (Eq. 3.12). For all the samples we find that $\ln(k_H)$ varies linearly with $1/T$, and an accurate estimate of $\Delta\dot{h}_0$ is obtained from the slope. Values of enthalpy in the zero coverage limit are summarized in Table A.2. The largest adsorption enthalpy (8.92 kJ mol^{-1}) is observed for ACF-10, which has the greatest fraction of narrow pores. In ACF-20, which has larger pore widths, the adsorption enthalpy (7.32 kJ mol^{-1}) is smaller. An intermediate enthalpy is observed for the activated carbon CNS-201.

The isosteric heat was calculated by fitting the 77 K and 87 K isotherms to the virial-type thermal equation (Eq. 3.8). As displayed in Fig. A.5, all of the samples are energetically heterogeneous, and the enthalpy decreases substantially with increasing n. Heterogeneity is especially pronounced for ACF-10. In the inset to Fig. A.5, the isosteric heat is also plotted against the fractional adsorption amount. When viewed as a function of fractional adsorption, the isosteric heat of ACF-10 remains higher than ACF-20 until a fractional

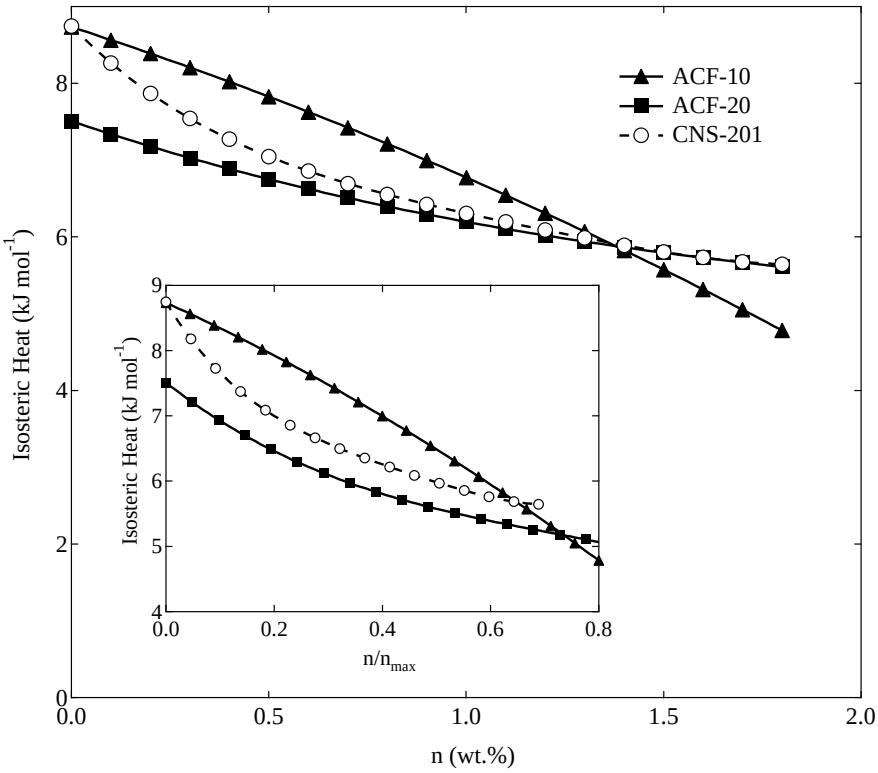

Figure A.5: The H_2 isosteric enthalpy of adsorption for ACF-10, ACF-20, and CNS-201 as a function of surface excess adsorption. Inset: The isosteric heat is plotted as a function of the fractional amount of adsorption (excess adsorption divided by the saturation adsorption amount at 77 K).

filling of about 0.7. For comparison between the different samples, the isosteric heats were averaged from $0\,\mathrm{mmol\,g^{-1}}$ to $9.5\,\mathrm{mmol\,g^{-1}}$, and these values are summarized in Table A.2.

A.4 Discussion

Heterogeneity in the adsorption potentials of microporous carbons is modeled using a distribution of widths of the slit pores. Recent studies have also stressed the importance of fluctuations in pore wall thickness on the adsorption potential [5, 129]. Narrow pores have deeper potential wells and should be filled at the lowest pressures. This is followed by the gradual filling of larger pores at higher pressures. At a given equilibrium pressure, p, there should be a critical pore width, below which all pores are filled and above which all pores

are vacant [73]. The zero coverage heat of H_2 adsorption, $\Delta\dot{h}_0$, reflects the initial filling of pores and therefore should depend on the PSD of the three samples.

Since ACF-10 contains a narrow peak at 5 Å in the PSD, the filling of these small pores presumably leads to the large zero coverage H_2 adsorption enthalpy. ACF-10 also contains a small fraction of wider pores, and it is the filling of these larger pores that apparently causes the steep decrease in the isosteric heat of adsorption at higher coverage. In ACF-20, there is a broad distribution of pore widths. In theory, the smallest 5 Å pores should fill first, leading to a similar zero coverage H_2 adsorption enthalpy as ACF-10. Measurements indicate, however, that ACF-20 has a significantly smaller zero coverage enthalpy than ACF-10. The exclusive filling of the smallest pores at low pressures, in isolation from the larger pores, may not be a realistic view. Simultaneous filling of pores with widths from 5 Å to 20 Å, on the other hand, might explain this smaller-than-expected zero coverage adsorption enthalpy. Therefore it is the relative abundance of the smallest pores relative to the larger pores which seems to have the greatest influence on the zero-coverage enthalpy.

In all three samples, the isosteric heat of adsorption decreases with the excess adsorption amount. Since the samples have different adsorption capacities, a better comparison can be made by plotting the isosteric heats as a function of fractional adsorption. This is displayed in the inset to Fig. A.5. The isosteric heats of both ACF-10 and ACF-20 decrease almost uniformly at low filling, but ACF-10 eventually falls below ACF-20 at a fractional filling of 0.7. At least some of the decrease in isosteric heat can be attributed to repulsive interactions between the adsorbed H_2 molecules. These unfavorable interactions are likely to be greater in small slit pores than in larger slit pores, leading to the observed behavior.

Heats of adsorption in the Henry's Law region (listed in Table A.2) are considerably greater than the 4–6 kJ mol^{-1} heats typically observed for H_2 adsorption on the surface of

carbon. This is due to strong interactions between adsorbed hydrogen molecules and the slit pore potential fields. Average isosteric heats of adsorption fall between 5.8–6.7 kJ mol^{-1} for the three samples, closer to the characteristic values for carbon. The H_2 adsorption enthalpy (ACF-10 > CNS-201 > ACF-20) is negatively correlated with the total H_2 adsorption capacity (ACF-20 > CNS-201 > ACF-10) for the three samples that were studied.

A.5 Conclusion

Pore size distributions and supercritical H_2 isotherms for two microporous activated carbon fibers and one coconut-derived activated carbon were measured and compared. The low surface area sample, ACF-10, has a narrow peak in the PSD at 5 Å with a very small tail at larger widths. The high surface area sample, ACF-20, has a broad PSD which contains widths from 5 Å to 20 Å and has a small positive skew. The coconut-derived activated carbon CNS-201 also has a broad PSD with widths from 5 Å to 20 Å. The zero coverage enthalpy of hydrogen adsorption depends strongly on the relative intensity of the smallest pore widths in the PSD. Zero-coverage enthalpies vary from 8.92 kJ mol^{-1} for low surface area ACF-10 to 7.63 kJ mol^{-1} for high surface area ACF-20.

Appendix B

Hydrogen absorption behavior of the ScH_2-$LiBH_4$ system

B.1 Introduction

Complex metal hydrides are basically salts consisting of an anionic complex $[MH_n]^-$ and a cation A^+ to balance the charge. Complexes containing light elements have been the focus of most research, due to their favorable gravimetric hydrogen densities. One such complex metal hydride is $LiBH_4$, which can release up to 13.8 wt% hydrogen by thermal decomposition:

$$LiBH_4 \longrightarrow LiH + B + \tfrac{3}{2}H_2. \tag{B.1}$$

Like most complex metal hydrides, $LiBH_4$ is a very stable compound. It requires temperatures well above 200 °C to release hydrogen. The standard reaction enthalpy is 61 kJ mol^{-1}, which translates to 1 bar equilibrium pressure at 400 °C [130, 131].

Chemical destabilization of $LiBH_4$ offers a versatile way to lower the desorption enthalpy [132–136]. Recent work has focused on adding an additional metal or metal hydride species which reacts to form a stable metal boride phase, lowering the overall reaction enthalpy.

Portions of this chapter were published in the article: J. Purewal, S. Hwang, R.C. Bowman, E. Rönnebro, B. Fultz and C.C. Ahn, *J. Phys. Chem. C* **2008**, *112*, 8481-8485.

Vajo et al. demonstrated that adding MgH_2 to $LiBH_4$ lowered the dehydrogenation enthalpy by $25\,kJ\,mol^{-1}$ [131]. Motivated by such successes, a comprehensive evaluation of potential chemically destabilized metal hydride systems was initiated, using density functional theory to evaluate formation and reaction enthalpies [137–139]. A significant result from this study was the identification of ScH_2 as a destabilizing agent with ideal thermodynamics [140]. The following decomposition pathway

$$ScH_2 + 2\,LiBH_4 \longrightarrow ScB_2 + 2\,LiH + 4\,H_2 \tag{B.2}$$

has a calculated reaction enthalpy of $34.1\,kJ\,mol^{-1}$ at room temperature. This system can release up to 8.9 wt% upon completion. An equilibrium pressure of 1 bar is calculated to occur at 57 ℃.

It is important to note, however, that first principles DFT calculations provide no direct information about either the reaction mechanism or the activation barriers. It is likely that the rate limiting steps would involve the breakdown of ScH_2 ($\Delta H_f = 200\,kJ\,mol^{-1}$) and the formation of ScB_2 ($\Delta H_f = 248\,kJ\,mol^{-1}$), both of which are stable compounds. While first-principles calculations have proved accurate in reproducing experimental PCT diagrams for the destabilized MgH_2-$LiBH_4$ system, it is uncertain whether similar success will be achieved for a system in which the reactant and product phases have considerably larger formation enthalpies. High energy ball-milling can improve reaction kinetics to some degree by reducing diffusion distances and increasing the concentration of reaction interfaces. It does not necessarily mitigate the large activation barriers to ScH_2 and ScB_2 decomposition however.

The aim of the present work is to experimentally investigate the importance of kinetic

barriers in determining hydrogen absorption and desorption behavior. Isothermal kinetic H_2 adsorption and desorption of the $ScH_2/LiBH_4$ system was measured at various temperatures. Reaction products were characterized using powder XRD, magic angle spinning NMR, and Raman spectroscopy. We were unable to verify the formation of ScB_2 in the product phase, and there was no evidence for the proposed reaction pathway (Eq. B.2). Rather, the $LiBH_4$ was found to decompose independently into LiH and amorphous boron without the reaction of ScH_2.

B.2 Experimental Details

Samples of ScH_2 were synthesized by heating small scandium pieces (99.9% purity, Standford Materials Corporation) in ultrahigh purity H_2 at approximately 350 °C. The resulting formation of scandium hydride was rapid and highly exothermic. This is illustrated in Fig. B.1, where the hydrogenation reaction is shown to complete within a minute or so. The large amount of released heat is evident from the spike in reactor temperature. Hydrogenation was allowed to proceed for 3 h to ensure equilibration. Volumetric analysis and X-ray diffraction both indicate that the reaction product is ScH_2. Roughly 10 g of a 2:1 molar mixture of $LiBH_4$ (95% purity, Sigma Aldrich) and freshly-prepared ScH_2 was loaded under argon atmosphere into a sealed 80 mL stainless steel vessel containing five 0.5 in. diameter stainless steel balls. The vessel was sealed with a rubber gasket and clamp and loaded into a planetary mill (Fritsch-pulverizette 6). Different mixtures were milled at 400 rpm for either 1 h or 10 h. For possible catalytic enhancement of the reaction rates, 2 mol% $TiCl_3$ (Sigma Aldrich) was added to several samples prior to milling. All samples were handled in argon atmosphere gloveboxes to prevent air and moisture contamination.

Isothermal kinetic desorption measurements were conducted on a custom built stainless

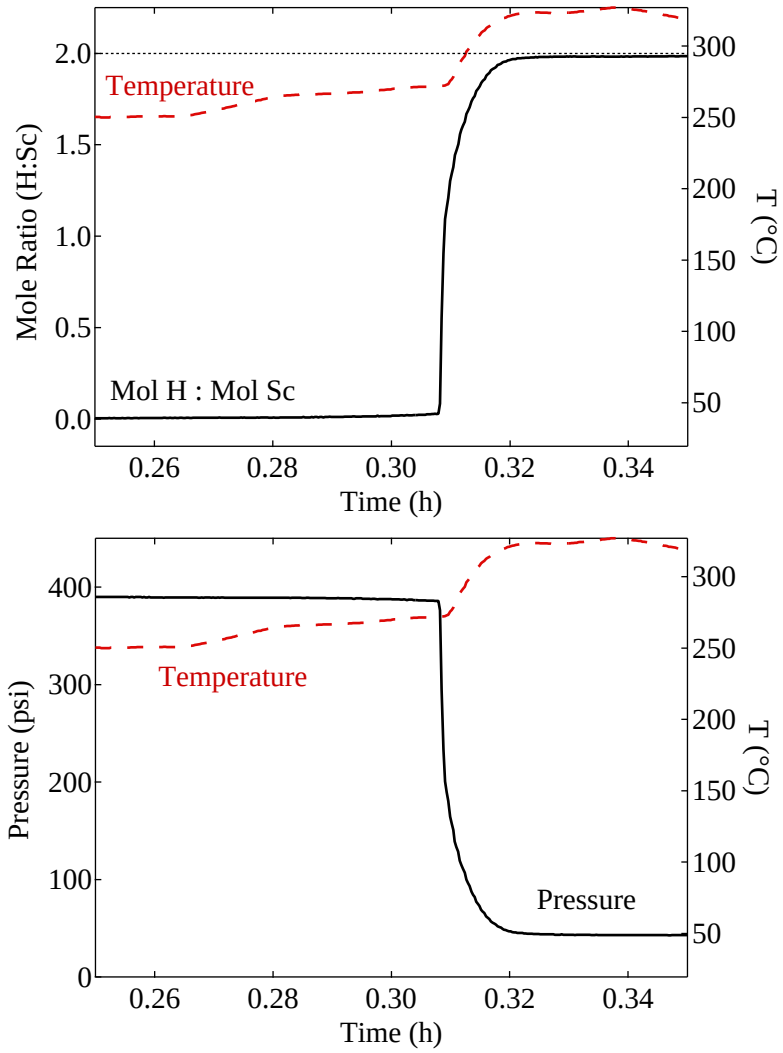

Figure B.1: Synthesis of scandium hydride. Top: Molar ratio of H to Sc in the solid scandium-hydrogen phase versus time. Bottom: Pressure of free H_2 in the reactor system versus time.

steel Sieverts apparatus. In a typical experiment, a 1 g sample was loaded into a 14 mL stainless steel reactor assembly sealed with a 0.5 in. Swagelok VCR filter gasket connection. The reactor was then mounted on the Sieverts system and enclosed in a thick, tight-fitting aluminum collar to maintain temperature uniformity. The furnace setup included a Watlow band heater fastened around the aluminum collar, with two thermocouples inserted into dedicated ports in the aluminum heat sink. The quantity of desorbed hydrogen was determined by volumetric measurements. Weight percents are reported with respect to the fully

hydrogenated samples, excluding the weight of the added catalyst. Powder XRD and Raman spectroscopy measurements were collected on samples sealed in 1.0 mm glass capillary tubes, following the procedure described in Sec. 2.6.

Solid-state magic angle spinning nuclear magnetic resonance (MAS NMR) measurements were performed using a Bruker Avance 500 MHz spectrometer equipped with a Bruker 4 mm boron-free cross-polarization (CP) MAS probe. The spectral frequencies were 500.23, 160.5, 121.6, and 73.6 MHz for the ^{1}H, ^{11}B, ^{45}Sc, and ^{6}Li nuclei, respectively. Samples were loaded into 4 mm ZrO_2 rotors, and each was sealed with a tight-fitting kel-F cap under argon atmosphere and spun at 13 kHz. The one-dimensional ^{11}B, ^{45}Sc, and ^{6}Li NMR spectra were acquired after a short (0.5 μs) single pulse (i.e., $< \frac{\pi}{12}$ for ^{11}B) with application of a strong ^{1}H decoupling pulse of the two-pulse phase modulation (TPPM) scheme [141]. The NMR shifts were reported in parts per million (ppm) with respect to "zeroes" set to standard external references: tetramethylsilane (TMS) for ^{1}H, $BF_3{-}Et_2O$ for ^{11}B, 1.0 M LiCl aqueous solution for ^{6}Li, and 1.0 M $Sc(NO_3)_3{-}HNO_3$ aqueous solution for ^{45}Sc nuclei.

B.3 Results

The hydrogen desorption behavior for the as-prepared $ScH_2 + 2\,LiBH_4$ mixtures were studied with kinetic desorption measurements using a series of temperature steps (Fig. B.2). Samples were heated inside a 72 mL volume to a final temperature of 450 °C. For samples maintained at this temperature, there was a release of 4.5 wt% hydrogen over 20 h. This is roughly half of the theoretical capacity of 8.91 wt% predicted for Eq. B.2. Longer milling times resulted in a small enhancement of the desorption capacity (an increase of less than 0.5 wt%) with no observable change in desorption kinetics. The composition of the desorbed gas was sampled using a residual gas analyzer (SRS, model RGA200) and found to

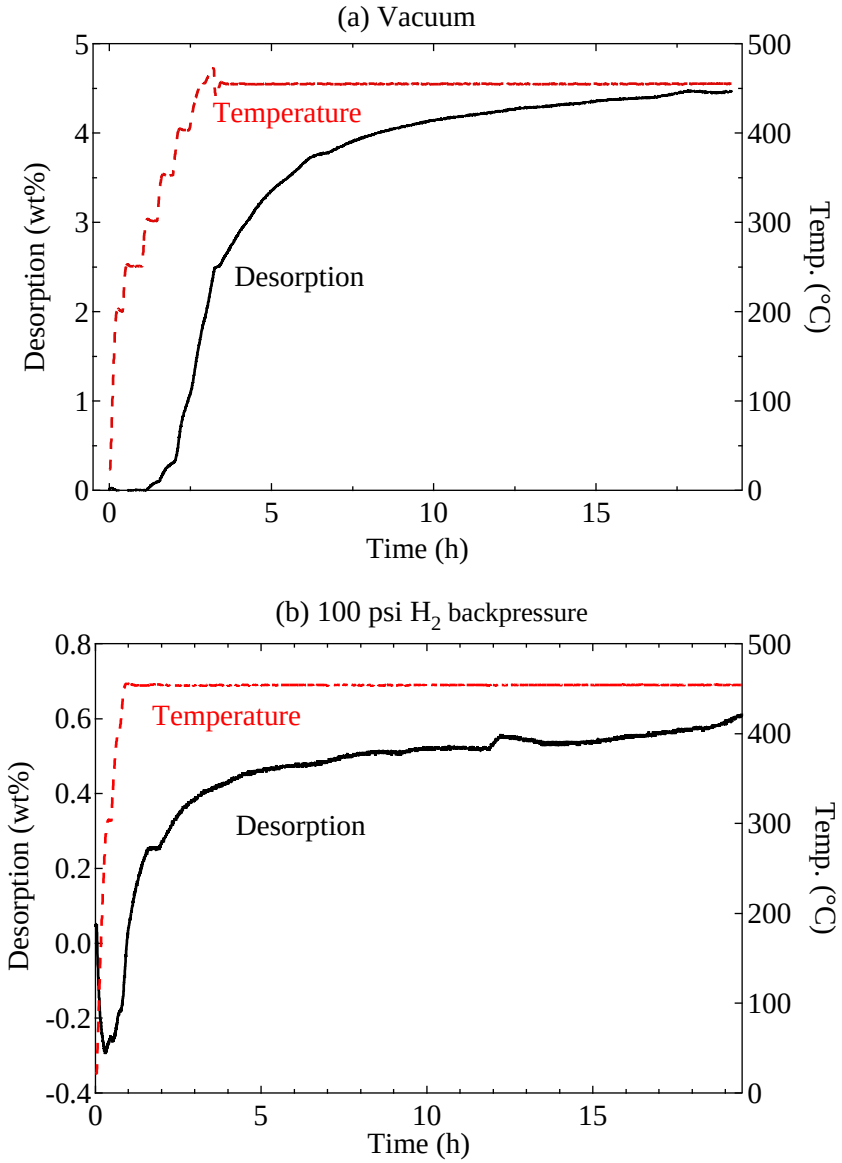

Figure B.2: Kinetic desorption data for the $ScH_2 + 2\,LiBH_4$ system. Top: Desorption into initially evacuated volume. Bottom: Desorption into 100 psi hydrogen backpressure.

contain over 99% hydrogen. Significant hydrogen desorption began at 350 °C, close to the temperature range at which the thermal decomposition of $LiBH_4$ is known to occur [142]. The 4.5 wt% of H_2 released at 450 °C is consistent with decomposition due solely to $LiBH_4$.[1]

Desorption measurements were also performed with an initial hydrogen backpressure of 100 psi, which was not found to enhance kinetics or to increase the hydrogen gas yield. Desorption from a $ScH_2 + 2\,LiBH_4 + 0.02TiCl_3$ sample was studied to assess the effect of a Ti catalyst on the reaction kinetics. At 280 °C, the desorption capacity was increased five-fold in the Ti-containing sample compared to the uncatalyzed sample. It should be noted that overall desorption capacity was still low, at 0.5 wt%. However, at 350 °C and 450 °C, the presence of $TiCl_3$ did not enhance either the kinetics or capacity.

The reverse direction of Eq. B.2 was also studied. A ball-milled $ScB_2 + 2\,LiH + 0.02TiCl_3$ sample was prepared and its hydrogen adsorption properties were studied. Starting with a 135 bar hydrogen pressure, a 0.8 g sample was heated to 300 °C for 48 h. No statistically significant hydrogen uptake was determined from a volumetric analysis. Powder XRD and MAS NMR analysis also failed to detect the formation of the expected product phases: $LiBH_4$ and ScH_2. A subsequent absorption experiment was performed with an 896 bar hydrogen pressure, with the sample kept at 460 °C for 48 h. A ^{11}B MAS NMR spectrum (see Fig. B.4a) of this sample revealed the presence of a small peak at -41 ppm, indicating a very limited $LiBH_4$ formation (about 3 mol%) in the reaction product. We note, however, that this pressure falls well out of the range of interest for technologically relevant metal hydride storage systems.

Figure B.3 shows the powder XRD measurements of the $ScH_2 + 2\,LiBH_4$ system before milling, after milling for 10 h, and after desorption at 450 °C for 20 h. The XRD pattern of

[1] Excluding the mass of the unreacted ScH_2, this would give 9 wt%, which is consistent with desorption measurements taken on unmixed $LiBH_4$.

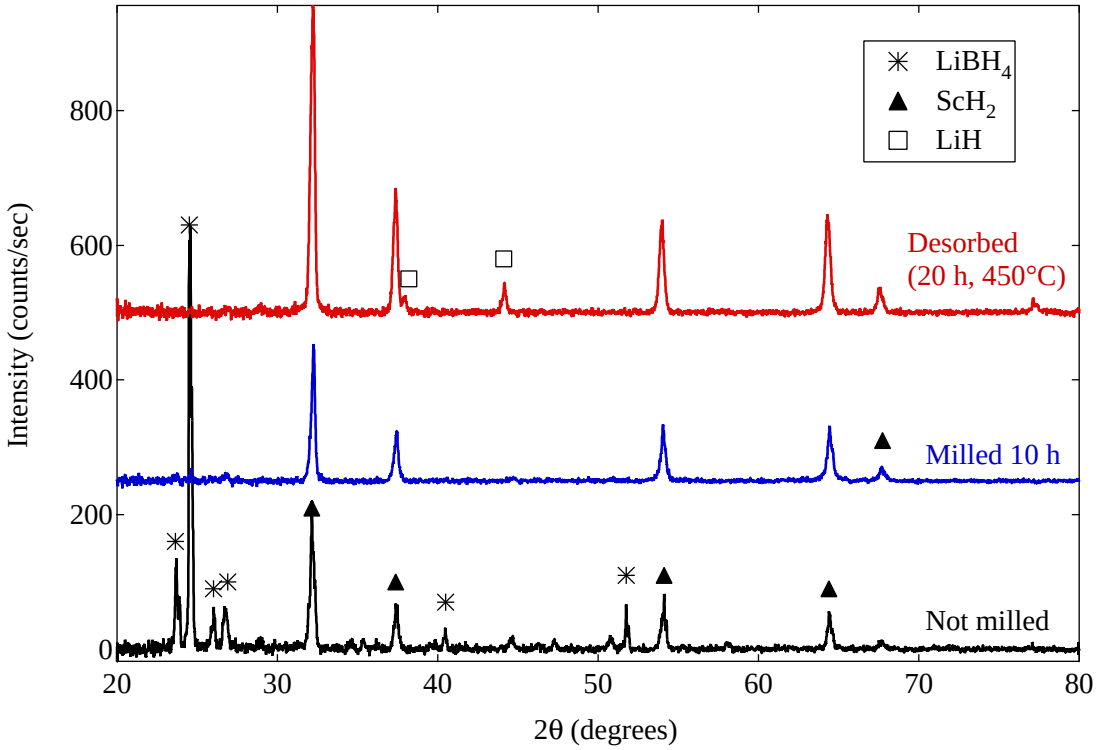

Figure B.3: Powder X-ray diffraction patterns for the $ScH_2 + 2\,LiBH_4$ system: before milling; after milling for 10 h; and after desorption at 450 ℃ for 20 h. Peak assignments were made with ICDD PDF2 card data for known or expected phases, including $LiBH_4$, ScH_2, LiH, ScB_2, Sc, and B.

the 450 ℃ desorption product reveals the presence of LiH and unreacted ScH_2. Since LiH is also an expected decomposition product of unmixed $LiBH_4$ [142], this does not provide evidence that the ScH_2 has participated in the reaction. A large background was also present due to the abundance of amorphous phases, presumably originating from the melting and re-solidification of $LiBH_4$ as well as from the formation of amorphous intermediate phases [143]. No peaks from the expected ScB_2 phase could be detected in the desorbed material.

Because a large fraction of the desorption product was amorphous, MAS NMR was utilized to complement the powder XRD results. Figure B.4 shows the ^{11}B, ^{45}Sc, and ^{6}Li MAS NMR data for the $ScH_2 + 2\,LiBH_4$ system after milling and after dehydrogenation (450 ℃ for 20 h). From ^{11}B NMR spectra, no noticeable change of the $LiBH_4$ peak was observed after ball-milling. The ^{11}B MAS and CPMAS spectra (Fig. B.4a and b) show the

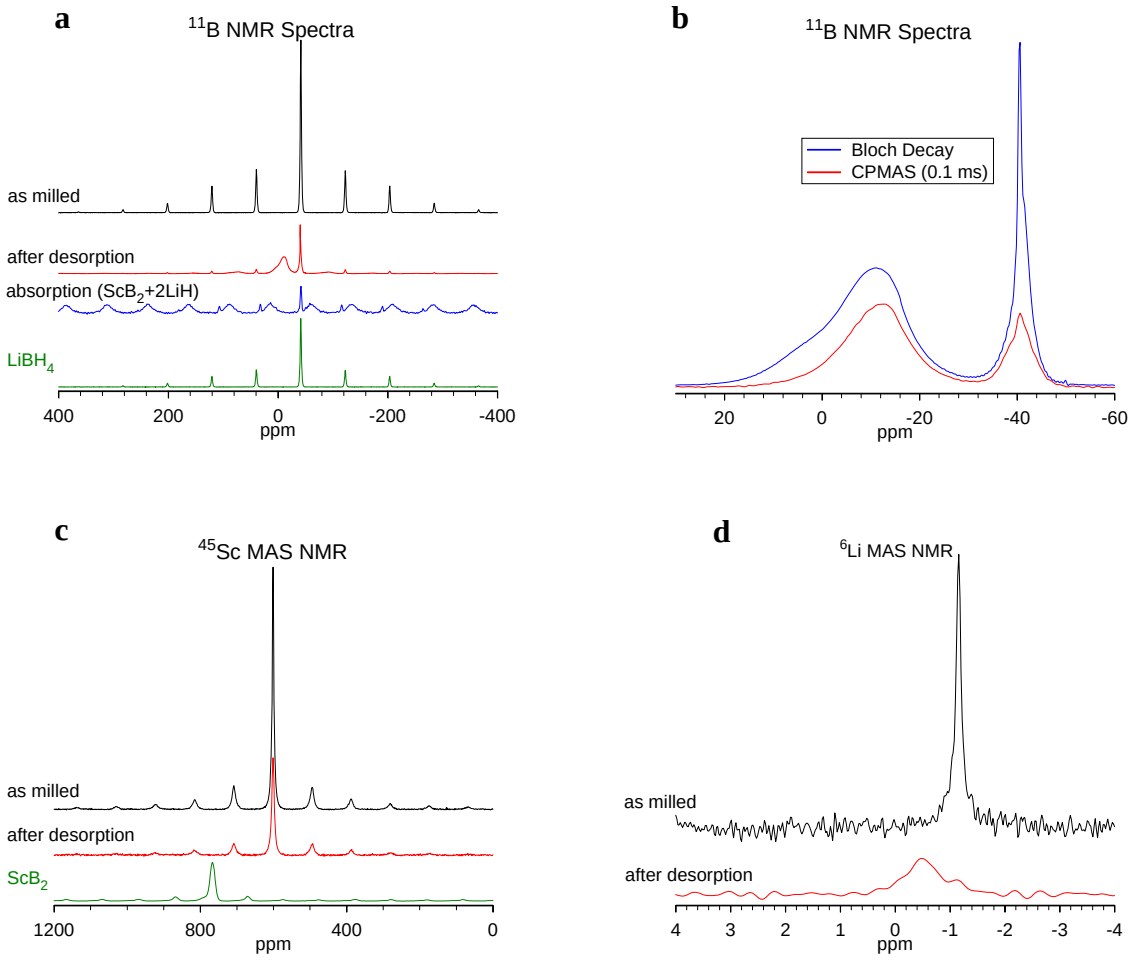

Figure B.4: NMR spectra of milled and dehydrogenated $ScH_2 + 2\,LiBH_4$. (a) Bloch decay ^{11}B MAS NMR spectra with neat $LiBH_4$ added as reference. Note that a spectrum of the $ScB_2 + 2\,LiH$ system after absorption treatment at high H_2 pressure (896 bar; see text) is also included, where the broader spinning sidebands in this spectrum are due to unreacted ScB_2. (b) ^{11}B MAS and CPMAS NMR spectra (contact time = 0.1 ms) of desorbed sample. (c) ^{45}Sc MAS NMR spectra with pure ScB_2. (d) ^{6}Li MAS NMR spectra

formation of elemental boron in the amorphous phase (broad shoulder at ~ 5 ppm) and the formation of an intermediate phase (with peak at -12 ppm) that was recently identified as an $[B_{12}H_{12}]^{2-}$ species [144]. We note also that some unreacted $LiBH_4$ is still present (seen from the peak at around -40 ppm) in the dehydrogenated product.

While unreacted ScH_2 is still present in the desorption products, ScB_2 is not detectable in the ^{45}Sc MAS NMR spectra presented in Fig. B.4c. Note that the ^{45}Sc signal was

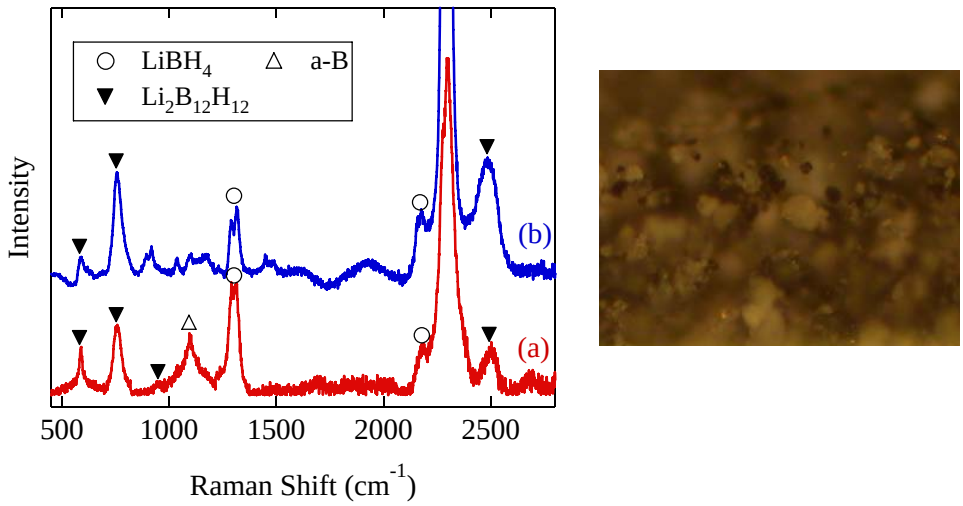

Figure B.5: Left: Raman spectra of the dehydrogenation products of (a) ScH_2+2 $LiBH_4$ system and (b) neat $LiBH_4$. Spectrum (a) corresponds to the white particles shown in the optical micrograph. The solid down-triangle, open circle, and open up-triangle identify Raman modes from $Li_2B_{12}H_{12}$, $LiBH_4$, and amorphous boron, respectively. Right: Optical micrograph of a $ScH_2 + 2\,LiBH_4$ system after desorption.

significantly reduced after the desorption reaction, which we tentatively attribute to the inhomogeneous separation of the solid ScH_2 phase and $LiBH_4$ melt, and the correspondingly nonuniform distribution of ScH_2 particles in the resulting NMR sample. The ^{6}Li MAS NMR spectra (shown in Fig. B.4d) also provide a distinctive signature of phase changes from $LiBH_4$ (-1.1 ppm) to $Li_2B_{12}H_{12}$ (-0.5 ppm). The presence of LiH was confirmed by independent ^{6}Li CPMAS NMR measurements (not shown) because extremely long spin-lattice relaxation behavior inhibited its observation during recording of the MAS spectra in Fig. B.4d. As with the XRD data, the NMR results identify the decomposition products of $LiBH_4$, but provide no evidence that ScH_2 has reacted to form the ScB_2 product.

Raman spectroscopy was used to probe the chemical composition of a $ScH_2 + 2\,LiBH_4$ mixture desorbed at 400 °C for 20 h. The results are shown in Fig. B.5. It was found that the desorption product segregated into two phases, which are visible in Fig. B.5 as white particles and dark particles. The dark particles and the as-milled $ScH_2 + 2\,LiBH_4$ mixture

did not have any Raman-active modes. However, the spectrum of the white particles bears a strong similarity to that of dehydrogenated $LiBH_4$. The B−H bending and stretching modes of $LiBH_4$ around $1300\,cm^{-1}$ and $2300\,cm^{-1}$ are present in both samples and, as observed previously, are not affected by decomposition at temperatures below 400 ℃ [143]. The broad peak at $1100\,cm^{-1}$ corresponds to vibrations in amorphous boron. The additional B−H bending and stretching modes around 500–1000 and $2500\,cm^{-1}$ are consistent with the calculated and measured B−H vibrational modes in $Li_2B_{12}H_{12}$ [145]. These results lead us to believe that the ball-milled $ScH_2 + 2\,LiBH_4$ mixture segregates back into its initial components upon the melting and solidifying of $LiBH_4$. The dark particles consist mainly of ScH_2, while the white particles consist mostly of $LiBH_4$ and its thermal decomposition products.

B.4 Discussion

The rate limiting steps of the absorption and desorption reaction of simple metal hydrides such as MgH_2 have been identified [146], but the reaction pathways of most destabilization-based reactions are still not well understood. Based on calorimetric and *in situ* XRD measurements, desorption in the $MgH_2 + 2\,LiBH_4$ system has been found to proceed in two distinct steps [147]:

$$MgH_2 \longrightarrow Mg + H_2 \tag{B.3}$$

$$Mg + 2\,LiBH_4 \longrightarrow MgB_2 + 2\,LiH + 3\,H_2. \tag{B.4}$$

An equivalent reaction pathway for the $ScH_2 + 2\,LiBH_4$ system would not work for the temperature range investigated here. Decomposition of ScH_2 does not occur until 900 ℃

[148, 149]. Well below this temperature, thermal decomposition of $LiBH_4$ should have already occurred independently. In principle, nanocrystalline ScH_2 may have a lower decomposition temperature due to excess surface energies and excess grain boundary enthalpies in the hydride phase. Reductions in the heat of formation of MgH_2 up to 30% have been estimated for crystallites smaller than 5 nm [150]. In practice, crystal grains with a minimum size of 10–15 nm are typically obtained with high energy ball-milling. Our own measurements of XRD peak broadening after ball-milling indicate an average ScH_2 crystallite size larger than 20 nm in the experiments. Moreover, the effect of nanocrystalline ScH_2 is complicated by the fact that $LiBH_4$ melts at 280 °C. Our results indicate that, above this melting temperature, the milled $ScH_2 + 2\,LiBH_4$ mixture segregates back into distinct phases. Another important insight is obtained by studying the desorption of a $Sc + LiBH_4$ system, which does not require the initial dehydriding of ScH_2. Significantly, it has been found that this reaction results in the formation of ScH_2 rather than ScB_2 [136]. From these results, it can be summarized that ScH_2 is not effective in destabilizing $LiBH_4$. Until the reaction mechanism is better understood, there is no simple way to surmount the significant reaction barriers present in this system.

B.5 Conclusion

Hydrogen sorption studies were performed on the $ScH_2 + 2\,LiBH_4$ system, identified by first-principle calculations as having favorable thermodynamics. Our experimental results demonstrate that H_2 desorption is consistent only with independent decomposition of $LiBH_4$. Extensive spectroscopic characterization (XRD, MAS NMR, Raman) failed to detect the ScB_2 product of the destabilization reaction. Due to the stability of ScH_2 and ScB_2, activation barriers in both directions appear to inhibit the predicted reaction at tem-

peratures below 450 °C. Sluggish kinetics mean that the destabilization reaction is unfavorable compared to competing reactions such as the independent decomposition of $LiBH_4$. Application of a H_2 pressure of ~ 900 bar to a heated $ScB_2 + 2\,LiH$ mixture was found to yield a minimal amount (i.e., $\sim$ 3 mol%) of the desired $LiBH_4$ phase. Furthermore, our findings suggest that the ball-milled $LiBH_4$-ScH_2 mixture segregates back into $LiBH_4$-rich and ScB_2-rich phases, due to the melting of $LiBH_4$. There was no indication that $TiCl_3$ assisted the destabilization reaction, although there was an improvement in the desorption kinetics.